

IN PRESS

Three-dimensional Imaging of Single Isolated Cell Nuclei using Optical Projection Tomography

Mark Fauver and Eric J. Seibel

University of Washington Human Interface Technology Lab
Seattle, WA USA
mfauver@u.washington.edu eseibel@u.washington.edu

J. Richard Rahn, Michael G. Meyer, Florence W. Patten,
Thomas Neumann and Alan C. Nelson

VisionGate, Inc,
Gig Harbor, WA USA
rahn@visiongate3d.com meyer@visiongate3d.com patten@visiongate3d.com
neumann@visiongate3d.com nelson@visiongate3d.com

Abstract:

A method is presented for imaging single isolated cell nuclei in 3D, employing computed tomographic image reconstruction. The system uses a scanning objective lens to create an extended depth-of-field image similar to a projection or shadowgram. A microfabricated inverted v-groove allows a microcapillary tube to be rotated with sub-micron precision, and refractive index matching within 0.02 both inside and outside the tube keeps optical distortion low. Cells or bare cell nuclei are injected into the tube and imaged in 250 angular increments from 0 to 180 degrees to collect 250 projections. After the projection images are further aligned, the filtered backprojection algorithm is applied to compute the 3D image. For calibrating the isometric resolution resulting from the 3D imaging system, a modulation transfer function was calculated by comparing the fixed focus image of a typical cell nucleus to the extended depth-of-field image. To assess loss of resolution from fixed focus image to projection image to 3D reconstructed image, the 10-90% rise distance was measured for a dyed microsphere. The resolution was found to be 0.9 μm for both pseudoprojection and 3D reconstructed images. Surface and translucent volume renderings and cross-sectional slices of the 3D images are shown of a stained nucleus from fibroblast and cancer cell cultures with added color histogram mapping to highlight 3D chromatin structure.

©2005 Optical Society of America

OCIS codes: Microscopy (180.0180), Three-dimensional microscopy (180.6900), Medical optics and Biotechnology (170.0170), Cell analysis (170.1530), Medical and biological imaging (170.3880), Three-dimensional image acquisition (110.6880), Tomography (110.6960)

References and links

1. P.J. Shaw, D.A. Agard, Y. Hiraoko, and J.W. Sedat, "Tilted view reconstruction in optical microscopy, three-dimensional reconstruction of *Drosophila melanogaster* embryo nuclei," *Biophys. J.* **55**:101-110 (1989).

2. J. Bradl, M. Hausmann, B. Schneider, B. Rinke, and C. Cremer, "A versatile 2D-tilting device for fluorescence microscopes," *J. Microscopy* **176**(3): 211-221 (1992).
3. S. Kikuchi, K. Sonobe, L. S. Sidharta, and N. Ohyama, "Three-dimensional computed tomography for optical microscopes," *Opt. Commun.* **107**: 432-444 (1994).
4. P. Matula, M. Kozubek, F. Staier, and M. Hausmann, "Precise 3D image alignment in micro-axial tomography," *J. Microscopy* **209**(2): 126-142 (2003).
5. J. Sharpe, U. Ahlgren, P. Perry, B. Hill, A. Ross, J. Hecksher-Sorensen, R. Baldock, and D. Davidson, "Optical projection tomography as a tool for 3D microscopy and gene expression studies," *Science* **296**:541-545 (2002).
6. S. Kikuchi, S. Kazuo, and N. Ohyama, "Three-dimensional microscopic computed tomography based on generalized Radon transform for optical imaging systems," *Opt. Commun.* **123**: 725-733 (1996).
7. E.H.K. Stelzer and S. Lindek, "Fundamental reduction of the observation volume in far-field light microscopy by detection orthogonal to the illumination axis: confocal theta microscopy," *Opt. Commun.* **111**(5-6): 536-547 (1994).
8. S. Kawata, O. Nakamura, and S. Minami, "Optical microscope tomography. I. Support constraint," *J. Opt. Soc. Am. A*, **4**(1): 292-297 (1987).
9. V. Lauer, "New approach to optical diffraction tomography yielding a vector equation of diffraction tomography and a novel tomographic microscope," *J. Microscopy* **205**: 165-176 (2002).
10. R.O. Chamgoulov, P.M. Lane, and C.E. MacAulay, "Optical computed-tomography microscope using digital spatial light modulation," in *Three-Dimensional and Multidimensional Microscopy: Image Acquisition and Processing, XI*, J.-A. Conchello, C.J. Cogswell, and T. Wilson, eds., *Proc. SPIE* **5324**, 182-190 (2004).
11. T. Wilson and C. Sheppard, *Theory and Practice of Scanning Optical Microscopy* (Academic Press, London, 1984).
12. J.B. Pawley, Ed., *Handbook of Biological Confocal Microscopy*, 2nd Ed. (Plenum Press, New York, 1995).
13. R. Heintzmann and C. Cremer, "Axial tomographic confocal fluorescence microscopy," *J. Microscopy* **206**(1): 7-23 (2002).
14. G. Häusler, "A method to increase the depth of focus by two-step image processing," *Opt. Commun.* **6**(1): 38-42 (1972).
15. A.C. Kak and M. Slaney, *Principles of Computerized Tomographic Imaging* (IEEE Press, New York, 1988).
16. M. Fauver, E. J. Seibel, J.R. Rahn, F.W. Patten, and A.C. Nelson, "Micro optical tomography system," in *Three-Dimensional and Multidimensional Microscopy: Image Acquisition and Processing, XI*, J.-A. Conchello, C.J. Cogswell, and T. Wilson, eds., *Proc. SPIE* **5324**, 171-181 (2004).
17. S. Inoue and K. Spring, *Video Microscopy: the fundamentals* 2nd Ed. (Plenum Press, New York, 1997).
18. J.C. Russ, *The Image Processing Handbook*, 4th Ed. (RC Press, New York, 2002)
19. M.L. Barr and E.G. Bertram, "A morphological distinction between neurons of the male and female, and the behavior of the nuclear satellite during accelerated nucleoprotein synthesis," *Nature* **163**: 676-677 (1949).
20. D. Wittekind, E.R. Reinhardt, V. Kretschmer, and E. Zipfel "Influence of staining on fast automated cell segmentation, feature extraction, and cell image analysis" *Anal. Quant. Cytol.* **5** (1): 55-60 (1983).
21. D. Zink, A.H. Fischer, J.A. Nickerson. "Nuclear structure in cancer cells" *Nat Rev Cancer* **4**(9):677-87 (2004).
22. J.D. Debes, T.J. Sebo, H.V. Heemers, B.R. Kipp, A.L. Haugen de, C.M. Lohse, D.J. Tindall. "p300 modulates nuclear morphology in prostate cancer" *Cancer Res.* **65**(3):708-12 (2005).
23. L. Vergani, M. Grattarola, C. Nicolini. "Modifications of chromatin structure and gene expression following induced alterations of cellular shape" *Int J Biochem Cell Biol.* **36**(8):1447-61 (2004).
24. G.S. Stein, M. Montecino, A.J. van Wijnen, J.L. Stein, J.B. Lian. "Nuclear structure-gene expression interrelationships: implications for aberrant gene expression in cancer" *Cancer Res.* **15**: 60(8):2067-76 (2000).

1. Introduction

With the introduction of three-dimensional (3D) X-ray CT imaging, the advantages of having cross-sectional views of human anatomy have revolutionized radiology. In an analogous approach using optical images taken up to 90-degrees apart, Shaw et al. (1989) reconstructed images from a single nucleus in 3D. However in practice, the ability to reconstruct 3D images of a cell nucleus from multiple and orthogonal perspectives have been fraught with technical challenges (Shaw et al., 1989; Bradl et al., 1992; Kikuchi et al., 1994). The previous attempts of rotating cells within a capillary tube appear to have been replaced by having the cells adhere to the outer surface of a spindle that is rotated (Matula et al., 2003). The technical challenges of 3D optical tomography are reduced for large multi-cellular specimens such as

embryos, and Sharpe et al. (2002) has demonstrated exquisite 3D images based on a custom turntable stage and low numerical aperture (NA) optics.

Since the acquisition of orthogonal views requires custom cell preparation techniques, a limited range of perspectives of the cell can be acquired using a fixed tube or the standard microscope slide. These techniques range from using one or more objective lenses (Kikuchi et al., 1996; Stelzer and Lindek, 1994) to scanning the illumination beam across the high numerical aperture of a single objective lens (Kawata et al., 1987; Lauer, 2002; Chamgoulov et al., 2004). Finally, a single perspective 3D image is acquired using laser scanning microscopy (Wilson and Sheppard, 1984), and most often in the confocal geometry (Pawley, 1995). However, the single perspective suffers from an anisotropic point spread function that suffers from severely curtailed spatial resolution along the optical axis, as compared to the lateral directions (Heintzmann and Cremer, 2002). In commercial confocal laser scanning microscope (CLSM) systems, image contrast is limited to fluorescence, which eliminates the direct comparison to cellular specimens prepared for standard histological and cytological purposes.

In our approach to developing the optical projection tomography microscope (OPTM), we chose to solve many of the optomechanical problems inherent in rotating individual cells and nuclei within a microcapillary tube. To generate 3D images with isotropic submicron resolution, the focal plane of a high NA objective lens is scanned axially through the cell nucleus to create a pseudoprojection. The capillary tube containing the fixed cell nucleus is rotated through 180 degrees during the acquisition of subsequent pseudoprojections, and the 3D reconstruction is computed using a filtered backprojection method commonly in x-ray computed tomography. By imaging in transmission, the resulting 3D image of the stained cell nucleus can be directly compared to knowledge base of pathologists and cytologists for diagnosing disease.

2. Methods

The optical projection tomography microscope is a modified brightfield transmission optical microscope (Olympus BX-51TF) with microcapillary tube-based rotation stage, which permits injection and viewing of cells radially around the full 360° of rotation. The refractive index matching both inside and outside the microcapillary tube minimizes optical distortion (that would otherwise be present due to the cylindrically-shaped tube). Another key feature is the piezoelectrically-driven objective lens positioner (Piezosystem Jena MIPOS-3 and NV40/1CL controller in closed loop mode) which allows the depth of field to be extended through incoherent superposition, in a manner similar to that described by Häusler (1972). The extension of the depth of field is necessary to form a suitable projection image, so that all features of the cell nucleus are present in equal focus from each different viewing angle. This is necessary for the purposes of tomographic reconstruction.

The Optical Projection Tomography Microscope

Figure 1 shows a schematic of the OPTM. In addition to the microcapillary-based specimen rotation stage and controller, and the piezoelectric objective lens positioner and its controller, there are position adjustments for rotation and translation of the CCD camera (Sensovation EZ-140m). These are used to align the microcapillary tube axis (axis of rotation) with the center line of pixels on the CCD, which facilitates reconstruction of the 3D image. A PC (Pentium 4, 2.4 GHz, Windows XP) running Labview™ (National Instruments) was used to generate and synchronize the control signals for the piezoelectric scanner and the camera trigger. Image data was acquired within Labview by calling the dynamic link library functions supplied by the camera manufacturer. Utilities added to the Labview-based control panel are determinations of the accuracy of rotational and translational camera adjustments, the measurement of camera grayscale histogram, and a routine to view all 250 projection images as a movie.

Microcapillary-based rotation stage

The microcapillary tube-based rotation stage consists of a 150 μm outer diameter, 50 μm inner diameter fused silica microcapillary tube (Polymicro) clipped into a microfabricated inverted v-groove fixture (Corning Polymer Gripper with glass substrate). Rotation is accomplished with a stepper motor (Newport SR50pp and ESP300 controller). Optical gel (Nye OC431A-LVP) was used to suspend the cell nuclei, and the same refractive index-matched optical gel was placed outside the microcapillary tube. Figure 2 illustrates the similarity between a standard slide-mounted specimen and the microcapillary tube-based viewing stage.

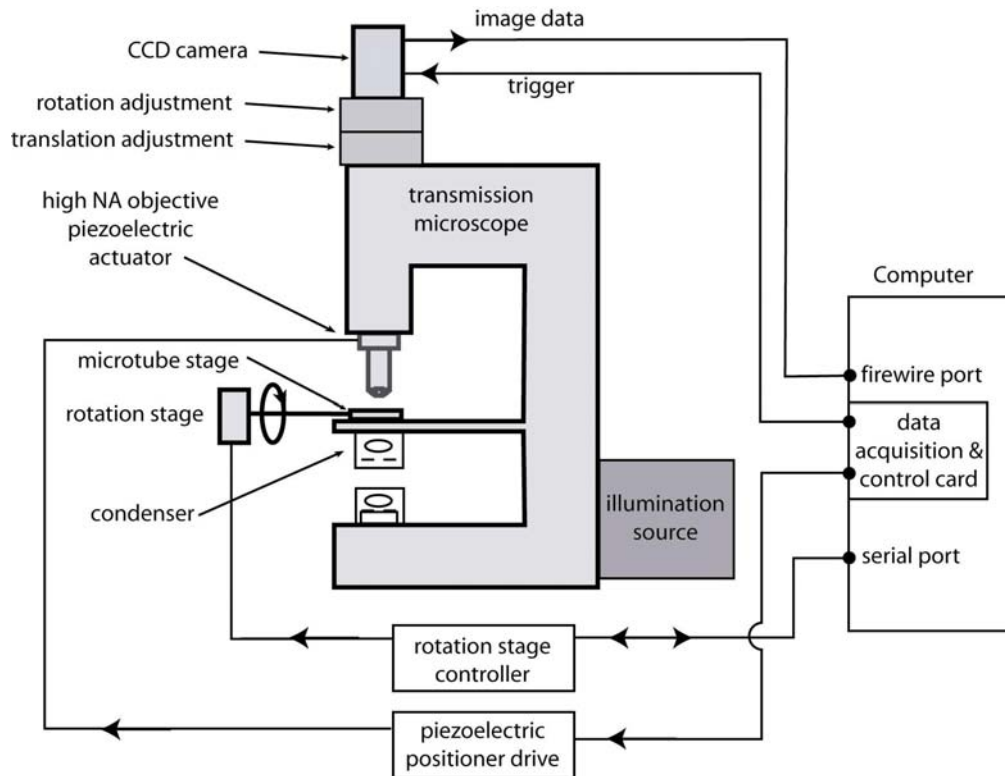


Figure 1: Schematic of Optical Projection Tomography Microscope (OPTM)

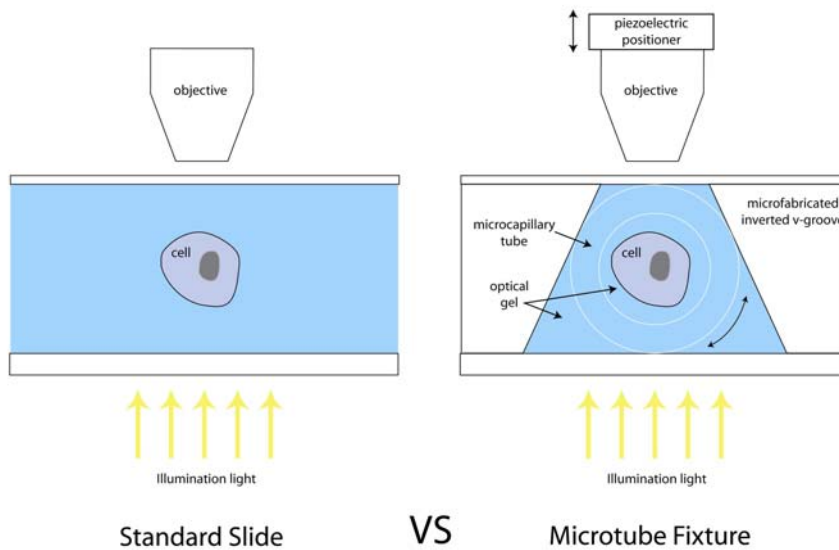


Figure 2: Comparison of standard slide mounting with microcapillary-based stage

Figure 3 shows the refractive index difference between the optical gel and the fused silica microcapillary tubing (Polymicro). The illumination is provided by a 100W quartz-tungsten-halogen lamp (Olympus), and filtered so that the majority of illumination power is from 500-700 nm in wavelength. The hematoxylin dye used to stain the cell nuclei has an absorption peak near 600 nm (Wittekind et al., 1983).

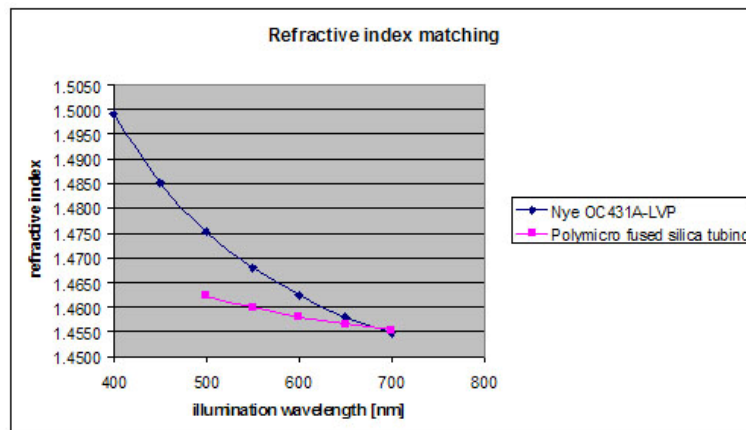


Figure 3: Refractive index differences versus illumination wavelength for the microcapillary-based viewing stage.

Projection image formation

In Figure 4 the method for projection image or pseudoprojection formation is shown. A high numerical aperture (NA) objective lens (Olympus 100x 1.25 NA plan C achromat) was used for imaging. The cell nucleus was scanned over a range of 10 μm . Doing so allows the camera to gather a high-NA, well-focused information from each focal plane within the 10 μm scan range, even though the depth of field (DOF) of the objective is only about 0.6 μm . Each image

plane is incoherently superimposed during acquisition to create a pseudoprojection, or shadowgram. All features in the pseudoprojections are uniformly defocused as a result, but the focused information for each feature is still present (assuming adequate sampling bit depth).

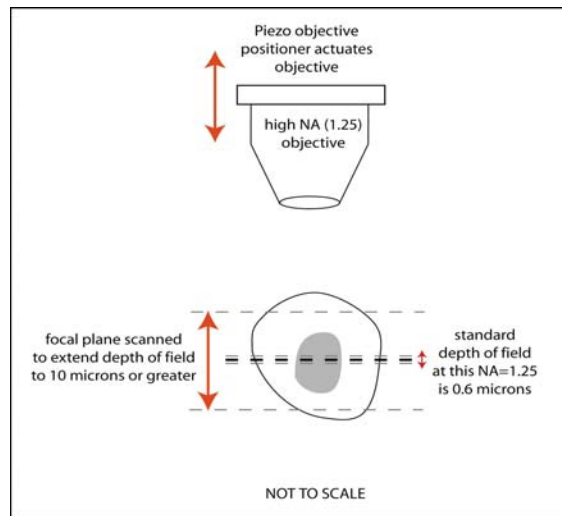


Figure 4: Extending depth of field for high NA objective to create a pseudoprojection

Post-acquisition image processing

After acquiring 250 pseudoprojections around 180° of rotation (angular interval of 0.72°), within 60 seconds, the object centers of the images are identified through segmentation and grey scale image processing algorithm, and each frame shifted to keep the cell nucleus from translating along the axis of the tube. This post-acquisition processing is employed for motion and registration correction, which is necessary to preserve the submicron tolerances required for a high quality tomographic reconstruction. Centration error is maintained by the instrument to the submicron range but additional correction, supplied by locating tube edges in software, is required to prevent centration artifact in reconstructions. Note that we currently do not correct for movement of the microcapillary tube perpendicular to the tube axis in the plane of the image. Any motion occurring along the optical axis of the microscope objective cannot be corrected for, thus it is of great importance that the microcapillary tube stage rotate with only sub-micron errors in this direction.

Visualization

After motion correction of the projection images along the direction of the microcapillary tube axis, the 3D image is computed using a filtered backprojection algorithm (Kak and Slaney, 1988). Our reconstruction uses cubic voxels, with a linear dimension of 0.0665 microns. We used a ramp filter to compensate for the rolloff in the sampling density, modulated with a Hann window to attenuate the effects of noise (Russ, 2002). After motion correction of the projection images along the direction of the microcapillary tube axis, the 3D image is computed using a filtered backprojection algorithm (Kak and Slaney, 1988). Our reconstruction uses cubic voxels, with a linear dimension of 0.0665 microns. We used a ramp filter to compensate for the rolloff in the sampling density, modulated with a Hann window to attenuate the effects of noise (Russ, 2002). The resulting 3D image is visualized using Volview™ (Kitware) after noise was reduced through filters selected within Volview. By adjusting the display settings within Volview, three different display modes were generated with 3D features being more easily understood when the specimen was rotated during viewing. These display modes were (1) surface rendering of the cell nucleus, (2) transparency of the surface to reveal inner nuclear structure, and (3) slice viewing from any viewpoint.

Sample Preparation

Samples from two cell lines, the lung fibroblast cell line CCD-34Lu and the A-549 lung-cancer cell line, were isolated and fixed. Cytoplasm was removed to yield bare cell nuclei, which were then stained with hematoxylin. The specimen was concentrated by centrifugation, and mixed with the optical gel. This cell-gel mixture is then injected under pressure into the microcapillary tube for viewing in the OPTM.

Calculation of the modulation transfer function

When we compute the power spectrum of the fixed-focal plane image, we first apply a 2D FFT to obtain a 2D map of spatial frequencies. In this map, all pixels located at the same distance from the central (DC) pixel have the same spatial frequency magnitude, but correspond to different directions. By finding the average of the values for each concentric circle, we obtain the power spectrum for each magnitude of the spatial frequency, independent of direction. By repeating this process with the pseudoprojection, and dividing the resulting power spectrum by that of the fixed focal plane image, we obtain an MTF.

$$MTF = \frac{\langle \|FT(image)\| \rangle_{angle}}{\langle \|FT(object)\| \rangle_{angle}} \quad (1)$$

where FT is the fourier transform, *image* refers to the pseudoprojection, and *object* represents the more ideal fixed focus image. The *angle* subscript indicates that we averaged each spatial frequency magnitude over all directions to reduce noise.

We can estimate the limit of resolution in an image by finding the spatial frequency at which the power spectrum exhibits a break in slope. For frequencies beyond this limit, the spectrum contains only noise (Russ, 2002).

Microsphere imaging and the 10-90% rise distance test

A microsphere-gel mixture was also fabricated using black-dyed microspheres of 2 to 3 μm in diameter (Polysciences). The 10-90% intensity rise distance measurement was used to establish loss of resolution throughout the various steps in forming a 3D image, with the fixed focus image used as the reference. The rise distance method determines the sharpness of the edge as an indicator of resolution. Figure 5 shows an example trace and 10-90% rise distance measurement, where the user sets the upper and lower boundaries to define the 0% and 100% levels. The 10% and 90% levels are calculated and the data point closest to these values is extracted. The 10-90% rise distance test is applied to fixed focus image data, pseudoprojection image data, and all three axes of the reconstructed image. Comparisons are made between these three types of data from the OPTM.

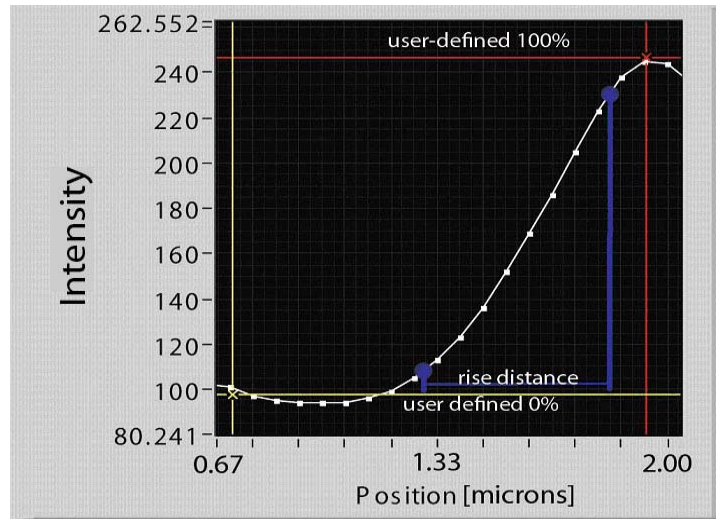


Figure 5: Example graph of 10-90% rise distance measurement

3. Results

Modulation transfer function and evaluation of resolution

The modulation transfer function (MTF) shown in Figure 7 was calculated from the image data shown in Figure 6. As the defocus becomes greater moving from a fixed focus image to a pseudoprojection image, we expect the power spectrum to shift towards the lower spatial frequencies. For a camera with a limited bit depth, this would eventually result in the loss of information about the spectral content at high spatial frequencies. As a test of the bit depth of our pseudoprojections, we acquired a pseudoprojection (10 μm integration range) and a fixed-focal plane image of a lung cancer nucleus (see Figure 6). We then calculated the ratio of the pseudoprojection's 2D power spectrum with that of the fixed-focal plane image. The resulting MTF, shown in Figure 7, reaches a minimum at around 1.1 linepairs/ μm , corresponding to a maximum spatial resolution of roughly 0.9 μm . For higher spatial frequencies, the ratio rises to a value near one; we interpret these higher frequencies as noise, which is expected to have equivalent spectral content in both images.

This MTF result is somewhat ambiguous, since some features being sampled (at varying degrees of focus) in the pseudoprojection are not present (except as defocused features) in the fixed focal plane image. Examination of the power spectrum of the fixed-focal plane image indicates that it contains spatial frequency signals up to roughly 2.5 linepairs/ μm . The ratio of the two images, plotted in Figure 7, shows that spatial frequencies as high as 1.1 to 1.2 linepairs/ μm are reproduced in the pseudoprojection, even for an integration range of 10 μm .

We also plotted the ratio of the fixed-focal plane image with a pseudoprojection acquired using a 20 and a 40 μm integration range (dashed and dotted lines in Figure 7, respectively). In this case, the usable spatial frequency limit is about 0.8 linepairs/ μm , which is equivalent to a spatial period of 1.25 μm . A reduction in the upper frequency limit is expected for a greater integration range.

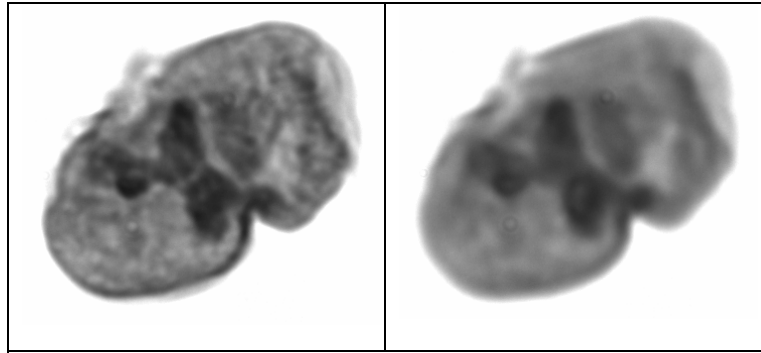
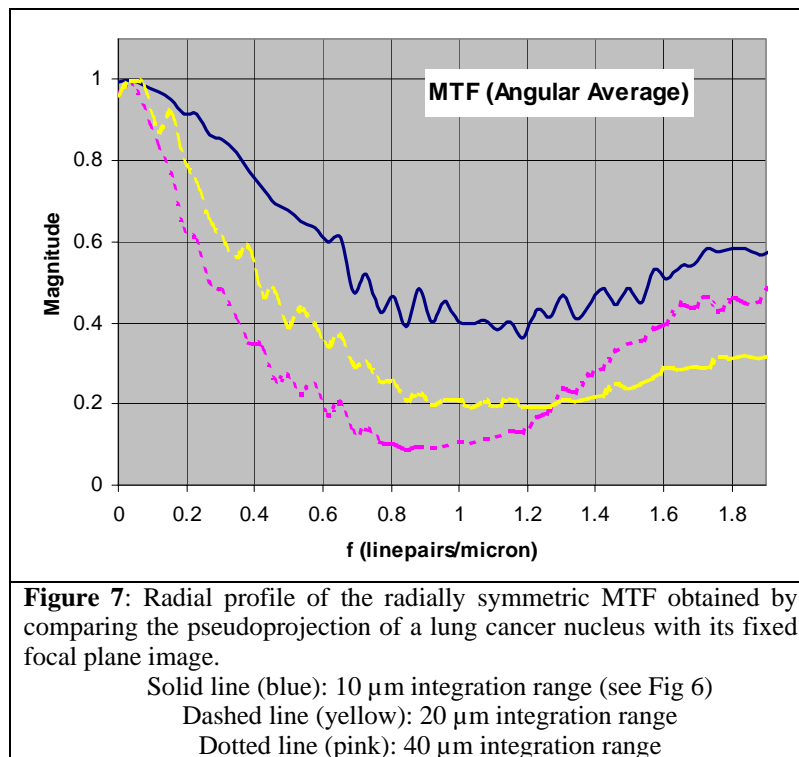


Figure 6. A lung cancer nucleus: the pseudoprojection (10 μm focal range; right) and the fixed-focal plane image (left) used for comparison



The 10-90% rise distance and evaluation of loss of resolution

Using the 10-90% rise distance test, the measurements on fixed focus images, pseudoprojections, and 3D reconstructed images of a dyed microsphere are presented in Table 1. Note that there appears to be loss of resolution as indicated by the difference in the 10-90% rise distance for fixed focus images compared to the pseudoprojections. However, there appears to be no significant difference between the pseudoprojections and the reconstructed image in this regard. The 10-90% rise distance is equal for all three axes of the 3D reconstruction, indicating that the resolution is isometric. Note that no deblurring was

performed on this data, and the only filtration comes from the filtered backprojection algorithm used to reconstruct the 3-D image.

The measurement of diameter of the microsphere in the fixed focus image also gives us our standard for comparison to other image types. The average diameter for fixed focus microsphere images is 2.50 μm , whereas the average of microsphere pseudoprojections is 2.56 μm , and the average of all diameters measured from the 3D reconstruction is 2.82 μm . The larger diameter as measured in the 3D reconstruction is primarily due to registration errors that cause feature broadening. The diameter of the microsphere as measured from the surface render is significantly larger because the threshold for surface rendering was chosen to be just above background noise level, and not at the half-maximum intensity level. Additionally, the diameter of the microsphere was measured in every possible dimension to assess feature distortion. The 3D surface rendering of the microsphere, mentioned at the bottom of Table 1, is shown in Figure 8. The XYZ axes shown in Figure 8 correlate with the XY, XZ, and YZ planes referred to in Table 1. The Z axis physically corresponds to the axis of the microcapillary tube (axis of rotation), and the XY plane is the plane of reconstruction.

Image Type	Measured microsphere diameter FWHM (μm)	Microsphere edge 10-90% rise distance (μm)
Fixed focus image (along tube axis 0°)	2.54	0.33 \pm 0.07
Fixed focus image (perpendicular to tube axis 0°)	2.45	0.44 \pm 0.07
Single pseudoprojection (along tube axis 0°)	2.50	0.53 \pm 0.07
Single pseudoprojection (perpendicular to tube axis 0°)	2.62	0.60 \pm 0.07
3D reconstruction (XY plane horizontal)	2.78	0.53 \pm 0.07
3D reconstruction (XZ plane horizontal)	2.89	0.53 \pm 0.07
3D reconstruction (YZ plane vertical)	2.78	0.53 \pm 0.07
3D surface rendering	3.42	N/A

Table 1: Diameter measurements and 10-90% rise distance for a single microsphere.

An orange coloration was used for the surface rendering of this microsphere in Figure 8, and virtual lighting is added using Volview to aid in depth perception.

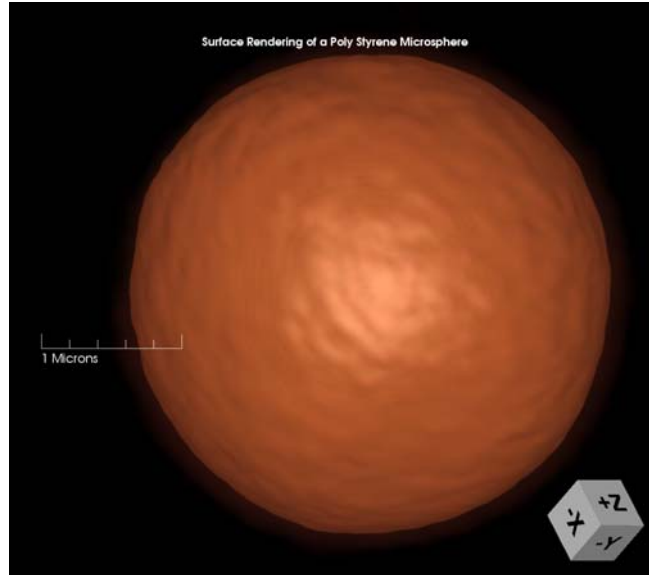


Figure 8 - (file: Msphere_022205_1741_Surface.avi 2.2MB)

Applying the Rayleigh criterion in equation 2 below gives us the theoretical minimum resolvable distance:

$$D = 1.22\lambda / (NA_{obj} + NA_{cond}) \quad (2)$$

where D is the minimum resolvable difference, taken to be “resolution”. λ is the wavelength of illumination, NA_{obj} is the numerical aperture of the objective lens, and NA_{cond} is the numerical aperture of the condenser lens.

Inserting our values for objective and condenser NA (1.25 and 0.2 respectively), and the average wavelength of illumination (0.60 μm), we calculate the minimum resolvable distance to be 0.50 μm . Because the minimum resolvable distance is a function of the separation of two peaks, and the 10-90% rise distance relates the sharpness of a single peak edge, the two are not directly comparable. The complex shape of the intensity peaks in real images precludes an exact relationship between the two measures of resolution. However, the Rayleigh criterion specifies that the maximum of one peak occupies the same position as the minimum of the second peak. If we apply this to our edge intensity data (as used in the 10-90% rise distance measurement), we find the peak separation to be $0.93 \pm 0.03 \mu\text{m}$.

Cell nucleus images

Figure 9 is a movie of a fibroblast cell nucleus, with the surface rendered as translucent so that internal structures are partially visible when coded in bright color. The images are color-coded as according to the vertical look-up table bar, with 255 equaling greatest absorption of transmitted light. All subsequent color movies in Figures 10-12 may differ in the exact assignment of color values. Coloration is used to aid visualization of internal nuclear structures, with particular color bands associated with cytologically relevant features, such as the Barr body (Xi chromosome) in orange (see Discussion). Figures 9-12 all use a pseudoprojection integration range of 10 μm .

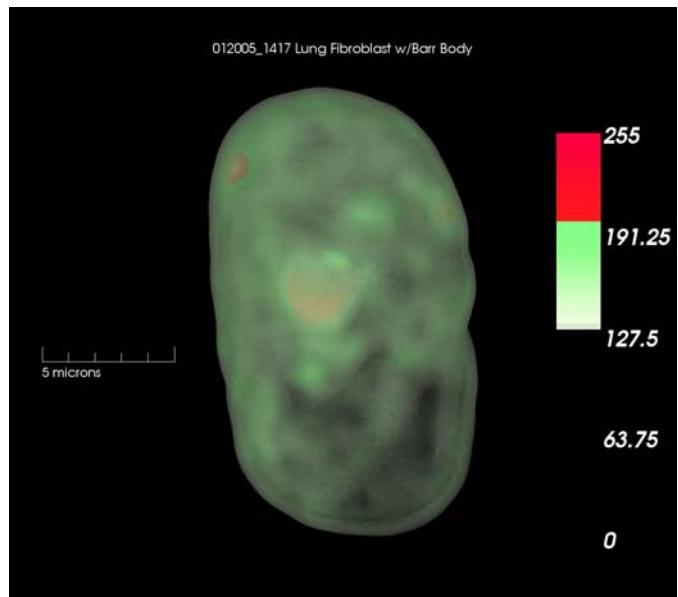


Figure 9: (file: NewTranslucent.avi 5.1MB)

Figure 10 is a movie of the same fibroblast nucleus shown in Figure 9, but in a thick slice (2.66 μm thick).

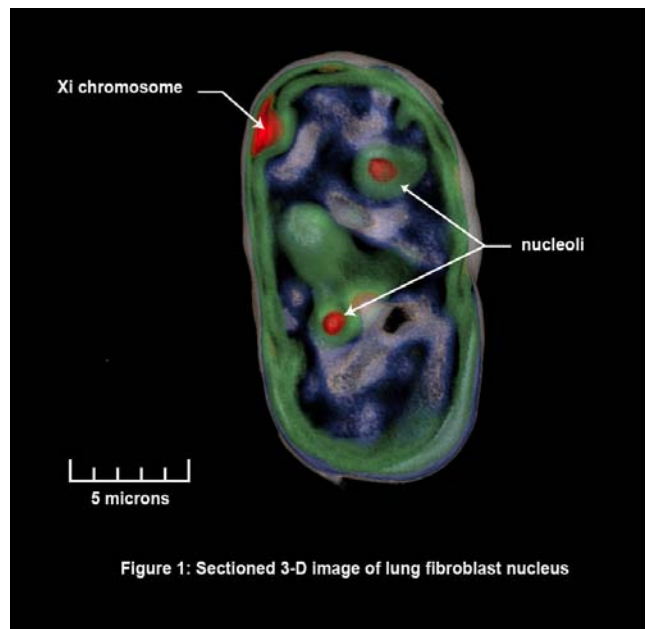


Figure 10: (file:012005_1417_BarrBodySlice.avi 3.2MB)

Figure 11 is a movie of a A-549 type cancer cell nucleus, with the surface rendered reflective. Virtual lighting is added using Volview to aid in depth perception.

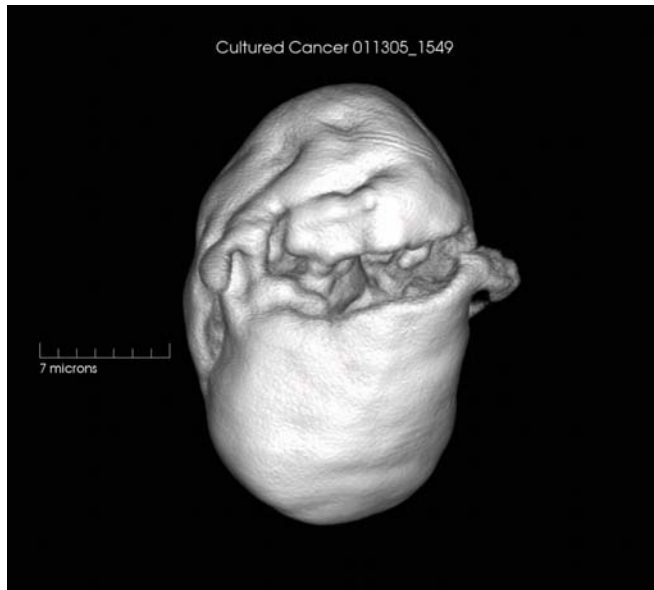


Figure 11: (file: Cancer2_011305_1549_A549_Surface.avi 2.9MB)

Figure 12 is a movie of the same cancer cell nucleus shown in Figure 11, but in a thick slice (1.7 μm thick).

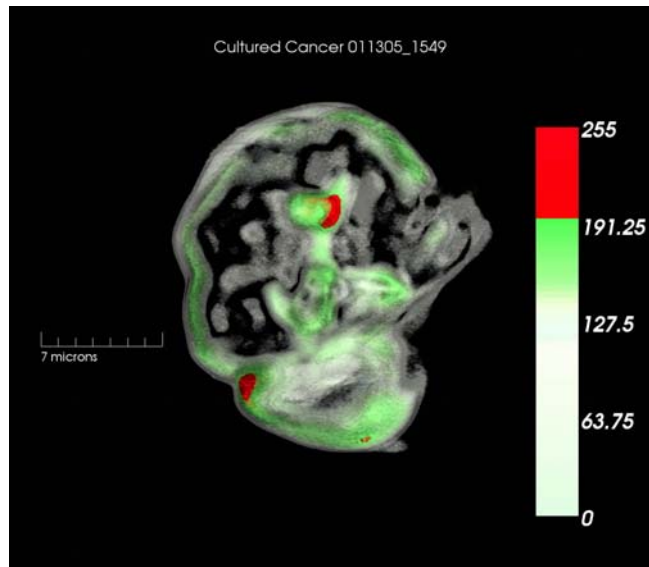


Figure 12: (file: Cancer2_011305_1549_A549_Slice.avi 3.0MB)

4. Discussion

By solving many of the fundamental problems with sample preparation and imaging in a rotating tube, high resolution 3D images of isometric resolution can be acquired using a conventional brightfield transmission microscope. Previous attempts such as Fauver et al., (2004) had residual registration errors in the range of 5 to 10 μm , which discouraged any attempt at sub-micron resolution. The recent advances in the optomechanics are the high degree of refractive index matching inside and outside the microcapillary tube, the microfabricated rotational joint, and the choice of an optical gel as embedding medium. The sample preparation procedure uses a thixotropic optical gel that requires high pressures to insert the gel-specimen mixture which remains quite stable with pressure removed.

The difficulty of inserting a test target into the microcapillary tube required a rethinking of methods to quantify resolution of the OPTM. The combination of two different methods, the MTF and the edge intensity profile-based measurements, lends more confidence that the system resolution is about 0.9 μm . Because the MTF measurement was performed on unfiltered data, there is no potential for artifact related to image filtration. The surface roughness exhibited in Figure 8 is interesting because it gives some qualitative indicator of surface render noise, assuming that the microsphere's surface is smooth. The 10-90% rise distance data for the reconstructed 3D image indicates that resolution is approximately equal along all three orthogonal planes. The rise distance values for the reconstructed 3D image are similar to that of the pseudoprojection. This implies that the filtration, used as part of the filtered backprojection algorithm to create the reconstruction, did not adversely affect the sharpness of the edge.

Future tests to be performed include the imaging of microsphere clusters. By varying the microsphere diameter to vary gap size between the microspheres, the resolvability of the each microsphere within the cluster could be established. Microsphere clusters may be used in the future to establish if the OPTM suffers from the feature overlap problem discussed by Pawley (1995) for confocal laser scanning microscopes that produce 3D images from only one perspective.

Biological significance

Figures 9 and 10 demonstrate initial results in feature identification in 3D reconstructions of cell nuclei. One feature selected for identification was the inactivated X-chromosome (Xi, also known as the Barr body). This structure is consistent throughout female mammalian somatic cells, and retains three distinct characteristics: (1) the diameter is approximately one micron, (2) the structure is connected to the inner surface of the nuclear membrane, and (3) the shape is pyramidal. Since the Barr body is expected to uptake the hematoxylin stain and have absorption contrast, no other observable structure in the cell nucleus is consistent with these criteria.

The Barr body has been first described by Barr and Bertram in 1949, and has been clinically used to implement rapid, non-invasive verification of gender. Cytological methods for Barr-body detection usually include the collection of cells from the test person (e.g. with a buccal swab), which are then spread on a slide, fixed and stained with hematoxylin. Since the cells are deposited on a slide in random orientation, only such Xi chromosomes that are coincidentally viewed from a proper angle will reveal the three characteristics of the Barr body, which is the case in only 5 - 20% of the cells. The aspect of random orientation is eliminated in the OPTM, where the sample (e.g. cell or nucleus) is rotated, and imaged in three dimensions. Thus, every single cell nucleus of a sample can potentially be identified as Barr-body positive or Barr-body negative.

The nuclear structure differs among cells of different type and transformation status. It is more and more accepted that nuclear architecture and spatial organization of the chromatin assembly play a critical role in the control of gene expression. (For a recent review see Vergani et al., 2004.) Although the underlying mechanisms are mostly unknown (Stein et al., 2000; Debes et al., 2005), changes in nuclear morphology are valuable indicators of certain

diseases, such as cancer. Cancerous cells exhibit typical alterations in nuclear morphology, which include changes in size, shape, and ratio of nucleus to cytoplasm, as well as changes in the nucleoli (Zink et al., 2004).

Morphological alterations in cancer nuclei are usually striking and identifiable with conventional 2D microscopy, without information about the true 3D arrangement of the chromatin. Conversely, nuclear changes in pre-malignant cells can be very subtle and difficult to detect. Here, 3D microscopy using the OPTM will help medical practitioners detect minute changes in nuclear structures, for example the appearance of the perinucleolar compartment (Zink et al., 2004), a structure of irregular shape with a highly variable size ranging from 0.25 to 1 μm in diameter. Our first application using the OPTM is the earliest possible detection of malignant and pre-malignant cells in a lung cancer screening program for persons at high risk, such as analyzing the sputum from previous smokers.

5. Acknowledgements

We would like to acknowledge the Washington Technology Center for providing seed funding, and the NIH/NCI SBIR program (Contract # HHSN261200433010C) for providing continuing funding for this work.

This project has been funded in whole or in part with Federal funds from the National Cancer Institute, National Institutes of Health, Department of Health and Human Services, under Contract No. HHSN261200433010C.

Thanks to Jeff Magula for assistance in design and fabrication of the microcapillary tube-based rotation stage.